The Role of Hydrothermal Carbonization in Sustainable Sodium-Ion Battery Anodes

Zhen Xu, Jing Wang, Zhenyu Guo, Fei Xie, Haoyu Liu, Hossein Yadegari, Mike Tebyetekerwa, Mary P. Ryan, Yong-Sheng Hu, and Maria-Magdalena Titirici*

Sodium-ion batteries as a prospective alternative to lithium-ion batteries are facing the challenge of developing high-performance, low-cost and sustainable anode materials. Hard carbons are appropriate to store sodium ions, but major energy and environmental concerns during their fabrication process (i.e., high-temperature carbonization) have not been properly assessed. Furthermore, the rational design of high-performing hard carbon anodes is usually limited by the conventional direct carbonization of organic precursors. Here, the hydrothermal carbonization process is employed as a versatile pre-treatment method of renewable precursors, followed by high-temperature carbonization, for producing advanced hard carbon anodes. The critical role of hydrothermal pre-treatment in regulating the structure for an optimized performance of hard carbon anodes is elucidated, while revealing the sodium-ion storage mechanism using electrochemical kinetic calculations, advanced characterization and multi-scale modeling. Furthermore, the environmental impacts of hydrothermal pre-treatment and subsequent carbonization are evaluated using life cycle assessment compared to direct carbonization. By comparing hard carbon anodes with and without the hydrothermal pre-treatment, it is verified that the additional hydrothermal process is responsible for enhanced electrochemical performance, increased carbon yields and reduced carbon emissions. The work provides a systematic understanding of functions and energy consumptions of hydrothermal systems to achieve next-generation sustainable sodium-ion batteries.

1. Introduction

The amount of lithium required for the predicted growth of lithium-ion batteries in the near future cannot be provided by current resources. Developing next-generation post-lithium battery technologies based on sustainable chemistry is therefore needed to deliver increased energy storage demands.[1] Sodium is an earth-abundant element with a similar redox potential to lithium, so sodium-ion batteries offer an attractive opportunity to become a sustainable complement to lithium-ion batteries, especially for grid energy storage or low-speed/short-distance electric transportation.[2] Nevertheless, the graphite anodes that dominate the commercial lithium-ion battery market cannot deliver the desired sodium-ion storage capacity. This means that the development of well-performing anode materials to store sodium ions is crucial.[3] In addition, the raw materials and fabrication processes of anodes need to be more sustainable than current graphite anodes which have been listed as a critical material for lithium-ion batteries.[3]

Z. Xu, Z. Guo, M.-M. Titirici
Department of Chemical Engineering
Imperial College London
London SW7 2AZ, UK
E-mail: m.titirici@imperial.ac.uk

J. Wang
Bristol Composites Institute (ACCIS)
School of Civil
Aerospace
and Mechanical Engineering
University of Bristol
Bristol BS8 1TR, UK

F. Xie, Y.-S. Hu
Beijing Key Laboratory for New Energy Materials and Devices
Beijing National Laboratory for Condensed Matter Physics
Institute of Physics
Chinese Academy of Sciences
Beijing 100190, China

H. Liu
Department of Chemical Engineering
Tsinghua University
Beijing 100084, China

H. Yadegari, M. P. Ryan
Department of Materials
Imperial College London
London SW7 2AZ, UK

M. Tebyetekerwa
School of Chemical Engineering
The University of Queensland
St Lucia, Brisbane 4072, Australia

M.-M. Titirici
Advanced Institute for Materials Research (WPI-AIMR)
Tohoku University
2-1-1 Katahira, Aobaku, Sendai, Miyagi 980–8577, Japan

Among all candidate anode materials, hard carbons have garnered the most interest because of their good reversible capacities of sodium-ion storage (around 250–300 mAh g^{-1}).[4,5] Unlike graphite, hard carbons consist of short-range graphitic domains and long-range amorphous features, where curved and defective graphene nanosheets turbostratically stack together with enlarged interlayer spacing.[6] In 2000, Steven and Dahn initially reported the usage of hard carbon anodes for sodium-ion batteries.[7] After that, scientists have widely developed hard carbons from various precursors including plastic, coal, biomass feedstocks, and petroleum products by direct carbonization, hydrothermal processes, microwave heating, spark plasma sintering, or a mixture of these steps for sodium-ion batteries.[8] However, most reported fabrication methods (e.g., direct high-temperature carbonization) face major energy and environmental issues, including low carbon yields, high energy consumption, and substantial carbon emissions.[9] In addition, some reported hard carbons are fabricated from fossil fuels rather than renewable resources,[10] which also questions the overall sustainability of such sodium-ion battery anodes. A promising hard carbon anode should be fabricated based on minimum energy consumption without depleting natural resources, whilst protecting the environment from emissions of carbon dioxide (CO_2) and other toxic chemicals.[11] As the majority of studies on hard carbon anodes for sodium-ion batteries entirely focus on the electrochemical performance but neglect the environmental impacts associated with their manufacturing,[12] how to enhance the sustainability of high-performance hard carbon anodes can be recognized as an overlooked but complex challenge. Furthermore, the detailed sodium-ion storage mechanisms within hard carbons remain a subject of debate.[13] Therefore, studies to further reveal the correlation between carbon structures and their electrochemical performance are essential in order to develop a rational design for advanced hard carbon anodes.

The hydrothermal carbonization process is widely used as a pre-treatment method to prepare hard carbons derived from renewable biomass.[14,15] Since research interests in sodium-ion insertion into hard carbons increased, the hydrothermal pre-treatment of biomass became particularly popular within the sodium-ion battery community.[16,17] Over the past 15 years, many scientists, including our group, have researched bio-derived hydrothermal carbons for energy conversion and storage containing sodium-ion batteries.[18,19] However, the role of hydrothermal pre-treatment in both the sustainability and performance of sodium-ion battery anodes has not yet been quantitatively analyzed, in comparison with the direct carbonization of the same precursors. Logically, an additional preparation step for carbon anodes involving a mild treatment temperature of 200 °C would imply extra energy consumption and increase carbon emissions. However, given the potential increased carbon yield and improved electrochemical performance provided by hydrothermal pre-treatment, real carbon emissions of hard carbons with and without this additional process need a specific assessment based on a normalized sodium-ion capacity.
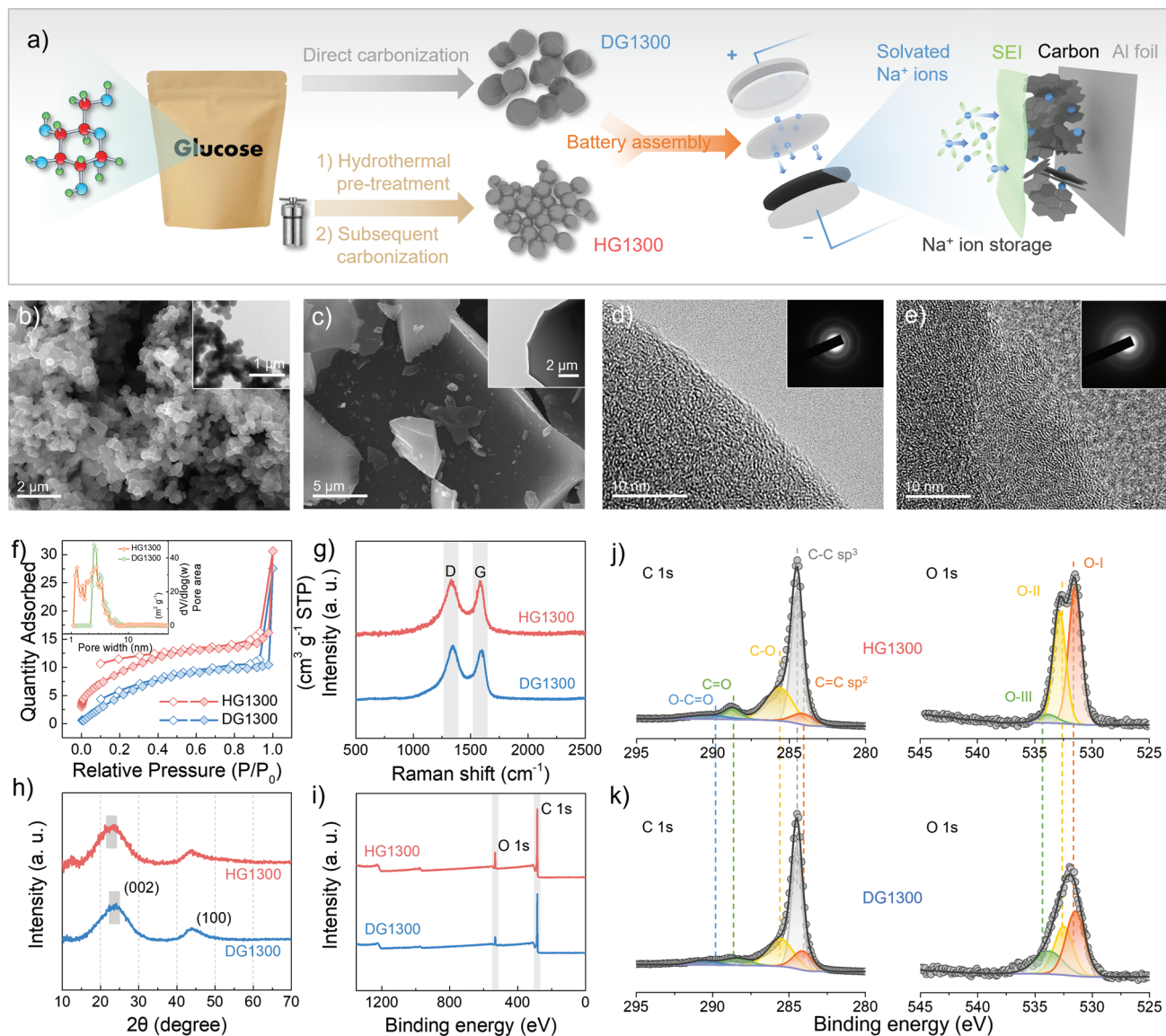
In this study, hard carbons were prepared either by the direct high-temperature carbonization of glucose or the hydrothermal pre-treatment of glucose followed by the high-temperature carbonization, establishing a comprehensive comparison platform. The structures and electrochemical performance of obtained hard carbons were characterized and correlated to unveil the sodium-ion storage mechanism and electrode-electrolyte interface properties, combined with electrochemical kinetic calculations, operando Raman spectroscopy, ex situ X-ray photoelectron spectroscopy (XPS), and multi-scale modeling (i.e., molecular modeling and finite element simulation). It is important to note that operando Raman characterization of hard carbons during the electrochemical sodium-ion storage, including the low-frequency Raman shift region, are complicated to perform due to their broad characteristic peaks with low intensities and the intense background caused by the Rayleigh scattering at the low-frequency Raman shift region.[20] Despite this, our design of the operando Raman cell has a remarkable resolution, making significant breakthroughs in achieving a real-time fine spectrum analysis of hard carbons. Meanwhile, through an innovative combination of life cycle assessment (LCA) with experimental testing of sodium-ion battery technologies, we can look across the different life-stages of hard carbon anodes from the supply chain of raw materials to the preparation of products and recycling of waste, thus assessing the differences in the sustainability of hard carbons with and without hydrothermal pre-treatment.[21] The hydrothermal pre-treatment confers more active sites (e.g., defects, closed nanovoids, etc.) into hard carbons to store sodium ions. The morphology of the hydrothermal carbon is spherical with hierarchical pore structures that facilitate a uniform ion flux and charge transfer. Also, the surface functional groups can help make the solid electrolyte interphase more homogenous, boosting the overall electrochemical performance. Moreover, the hydrothermal carbonization process can pre-stabilize the morphologies and structures of carbon materials to simultaneously increase the total carbon yield, specific capacity and thus decrease the carbon emission, overturning the traditional but unverified understanding that the hydrothermal pre-treatment as an additional step would increase the cost and carbon emissions of hard carbon anodes. Overall, we provide a systematic study to critically analyze and understand the contribution of hydrothermal pre-treatment to the electrochemical performance and sustainability of advanced hard carbon anodes for sodium-ion storage, which can provide guidance for rationally fabricating sustainable, high-performance sodium-ion batteries in the future. Only when sustainability exists at each stage can we achieve a promising battery technology towards carbon neutrality.[22]

2. Results and Discussion

2.1. Synthesis and Structural Characterization of Bio-Derived Hard Carbons

As illustrated in **Figure 1**a and Figure S1, Supporting Information, hard carbons were prepared using the hydrothermal pre-treatment of glucose at 200 °C for 12 h, followed by the high-temperature carbonization at 1000, 1300, or 1500 °C for 2 h under N_2 atmosphere, which has been well-optimized based on our group's previous research experience without using any additional chemicals.[23] Experimental details are

Figure 1. Material characterization. a) The schematic illustration of the two synthesis routes of glucose-derived hard carbons. One is the direct carbonization of glucose (DG), and the other is the hydrothermal pre-treatment of glucose at 200 °C (HG) followed by the high-temperature carbonization; SEM images with inserted TEM images of b) HG1300 and c) DG1300; HRTEM images with SAED patterns of d) HG1300 and e) DG1300; f) N_2 adsorption and desorption isotherms with the corresponding pore distributions, g) Raman spectra, h) XRD patterns, and i) XPS surveys, of HG1300 and DG1300; Fitted C 1s and O 1s core-level XPS spectra of j) HG1300 and k) DG1300.

listed in Supporting Information. The as-obtained carbon samples are denoted as HG1000, HG1300, and HG1500. In comparison, directly carbonized samples from the same precursor at different temperatures including 1000, 1300, and 1500 °C for 2 h are denoted as DG1000, DG1300, and DG1500, respectively.

First, the resulting carbons obtained through the hydrothermal pre-treatment and subsequent carbonization exhibit a uniform spherical morphology. The carbon spheres all have a similar diameter around 200 nm (Figure 1b and Figure S2, Supporting Information). During the hydrothermal process, the glucose molecules gradually dehydrate to form 5-hydroxymethylfurfural which polymerizes, nucleates, and form spherical hydrothermal carbons in the aqueous phase.[24] The subsequent

carbonization further introduces the conductivity and stabilizes the morphology. The compact packing density resulting from the unique spherical morphology can contribute to shorter diffusion pathways for ions and electrons (Figure S2, Supporting Information).[25] On the other hand, the directly carbonized carbons show a completely different morphology of irregular particles with different particle sizes according to the scanning electron microscopy (SEM) images (Figure 1c and Figure S2, Supporting Information). The direct high-temperature carbonization first results in the rapid foaming and expansion of precursors, followed by sintering, which finally produces disconnected carbon blocks. The morphological differences in obtained electrodes will be inherited from the carbon materials

(Figure S2, Supporting Information) to affect their electrochemical performance. Based on the high-resolution transmission electron microscopy (HRTEM) images (Figure 1d,e, and Figure S3, Supporting Information) and the corresponding selected area electron diffraction (SAED) patterns, the inner structures of carbon materials display both turbostratic and amorphous features, which means they are categorized as hard carbons.

N$_2$ adsorption and desorption isotherms can be employed to characterize the porosity of carbons. According to the isotherms in Figure 1f, the Brunauer–Emmett–Teller (BET) specific surface areas (S$_{BET}$) of HG1300 and DG1300 are 34.4 and 28.0 m^2 g^{-1}, respectively. The pore size distributions analyzed using the non-local density functional theory (NLDFT) method are inserted in Figure 1f, where hierarchical pore structures including micro- and meso-pores of HG1300 can be beneficial to mass transportation and ion diffusion.[26] In contrast, dominant mesopores but few micropores can be observed from directly carbonized DG1300. This phenomenon can also be seen from the isotherms of DG1000 and HG1000 (Figure S4, Supporting Information), where the surface area of HG1000 (338.8 m^2 g^{-1}) with abundant micropores is much larger than that of DG1000 (85.1 m^2 g^{-1}) with fewer micropores. Therefore, it can be concluded that the hydrothermal pre-treatment method can generate more micropores within carbons and thus increase the overall surface area when the carbonization temperature is constant.[27] With the carbonization temperature increasing from 1000 to 1500 °C, for each type, the surface areas of carbons decrease, while their average pore diameters increase (Table S1, Supporting Information). The difference in surface areas between 1000 and 1300 °C is the most prominent, indicating that the carbonization temperature of 1300 °C is a critical factor in decreasing the surface area due to the closure of most micropores at this temperature (Table S1, Supporting Information).[26] Consequently, HG1300 can possess more closed nanovoids than DG1300 (Figure S4, Supporting Information), which has also been confirmed in our previous studies using small-angle X-ray scattering (SAXS) and ^{23}Na solid-state nuclear magnetic resonance (NMR) spectroscopy of hydrothermal carbons.[23,28]
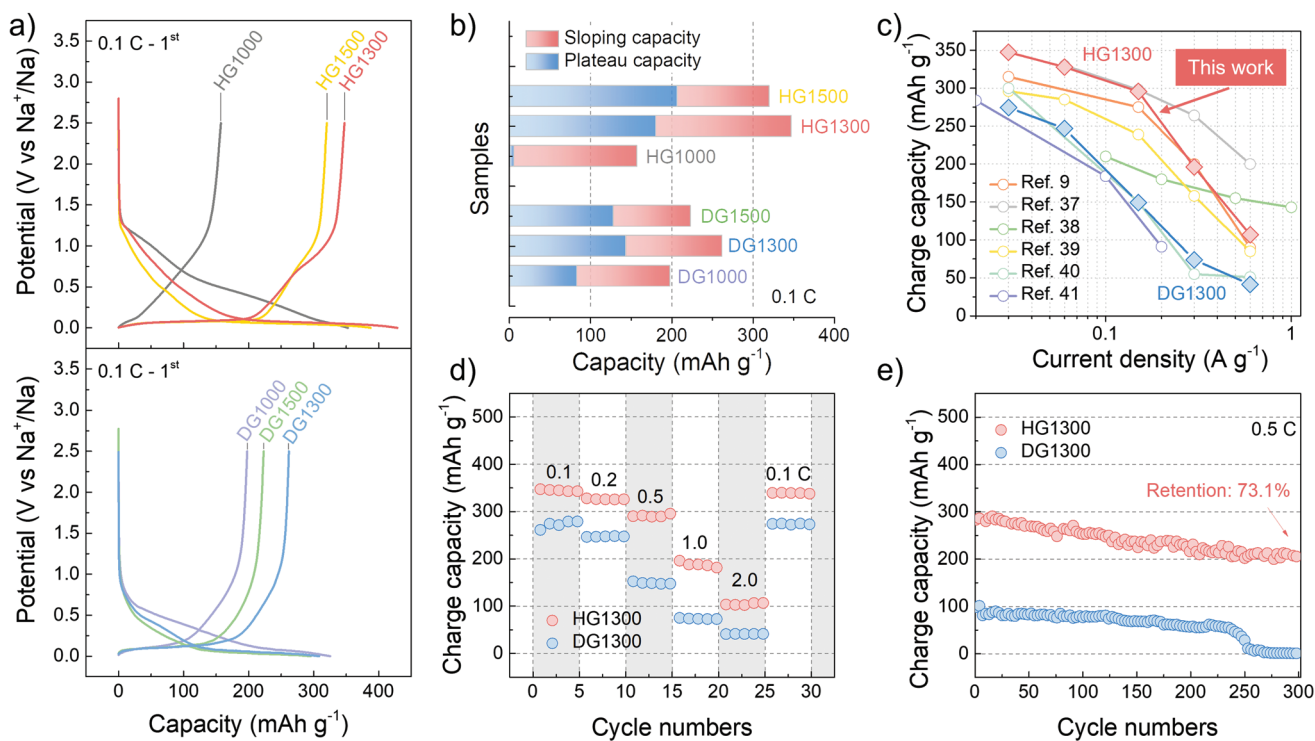
The defect structures of carbons can be studied with Raman spectroscopy, X-ray diffraction (XRD), and XPS. Raman spectra of HG1300 and DG1300 (Figure 1g) exhibit typical broad D- and G-peaks, further demonstrating they belong to disordered hard carbons classified as Stage II in the three-stage Raman model proposed by A. C. Ferrari et al.[29–32] In contrast to ordered graphitic carbons in Stage I such as graphite, graphene, and carbon nanotubes,[31] the intensity ratio of D- to G-peaks (I$_D$/I$_G$) of hard carbons in Stage II increases when the defect concentration of the curved graphene layers of hard carbons decreases (See Equation S1, Supporting information for further explanation).[30] Therefore, the lower I$_D$/I$_G$ value of HG1300 compared to that of DG1300 (Table S1 and Figure S5, Supporting Information) indicates more defective graphene planes in HG1300, suggesting that, the hydrothermal pre-treatment is responsible for the formation of more defects within carbons. With the increase in the carbonization temperature from 1000 to 1500 °C, the I$_D$/I$_G$ value increases, indicative of a less defective carbon structure (Table S1 and Figure S5, Supporting

Information). Furthermore, the defect structures described before can be further categorized into intrinsic and extrinsic defects.[33] XRD patterns (Figure 1h) can be used to selectively study the intrinsic defects caused by turbostratic graphene nanosheets. At the same time, XPS spectra can analyze the extrinsic defects created by the presence of heteroatom dopants on carbon surfaces (Figure 1i). XRD patterns of HG1300 and DG1300 both display two broad peaks located at $2\theta \approx 24°$ and 44°, attributed to the expanded (002) and (100) planes as well as the distortion and dislocation of lattices inside carbons. However, HG1300 is more disordered than DG1300; from the analysis of its calculated average interlayer spacing of (002) planes (d$_{002}$) being wider than that of DG1300 (Table S1, Supporting Information). In addition, the broader full width at half maximum of (002) planes (FWHM$_{002}$) of HG1300 also indicates less uniform carbon interlayer spacing (Table S1, Supporting Information). As the carbonization temperature increases from 1000 to 1500 °C, the carbon structure becomes more ordered because of the smaller corresponding values of d$_{002}$ and FWHM$_{002}$ (Table S1 and Figure S6, Supporting Information). Meanwhile, according to XPS surveys (Figure 1i) and fitted core-level XPS spectra (Figure 1j,k), the atomic amount of oxygen doping inside HG1300 and DG1300 can reach 9.8 at. % and 6.8 at. %, respectively, in which C=O carbonyl groups (O-I) and C—OH hydroxyl or C—O—C ether groups (O-II) dominate. Besides, the O-III peak representing the oxygen in carboxyl groups on the surface of our carbon materials can be also found. When the carbonization temperature increases from 1000 to 1500 °C, the amount of oxygen doping decreases (Table S1 and Figure S7, Supporting Information). To sum up the observations from experimental characterization, the hydrothermal pre-treatment leads to more defects (e.g., intrinsic carbon dislocation and vacancies, extrinsic oxygen doping, etc.) into hard carbons. Hence, the discrepancy in electrochemical results can be reliably ascribed to these physicochemical properties including the morphological, structural, and compositional variations of carbons and obtained electrodes, and the detailed characterization can provide deep insights into the role of hydrothermal processes in sustainable sodium-ion battery anodes.

2.2. Electrochemical Testing in the Half-Cell Configuration

The half-cell configuration can be applied to investigate the ability of hard carbons to store sodium ions. In this two-electrode configuration, the hard carbon electrode is utilized as the working electrode and placed against a piece of metallic sodium used as both the reference and counter electrodes. The half cells were tested from 0.001 to 2.5 V versus Na$^+$/Na using 1 M NaClO$_4$ in ethylene carbonate (EC) and dimethyl carbonate (DMC) (1:1 in volume) as the electrolyte.

The first cycles of galvanostatic charge/discharge (GCD) curves of hard carbons are shown in **Figure 2**a. Among them, HG1300 delivers the highest reversible charge capacity of 347.4 mAh g^{-1} at 0.1 C with both obvious plateau and sloping regions.[23] In comparison, the reversible charge capacity of DG1300 is only 261.3 mAh g^{-1}, which ranks the highest among the DG series. Hence, HG1300 and DG1300 from two different synthesis routes will be studied in detail as the most promising

**ADVANCED
SCIENCE NEWS**

www.advancedsciencenews.com

**ADVANCED
ENERGY
MATERIALS**

www.advenergymat.de

Figure 2. Electrochemical testing. a) The first cycle of GCD curves of different samples including HG1000, HG1300, HG1500, DG1000, DG1300, and DG1500 at 0.1 C (1 C = 300 mA g^{-1}) within the potential range of 0.001–2.5 V versus Na$^+$/Na using 1 M NaClO$_4$ in EC-DMC; b) The contributions of sloping and plateau capacities in each sample; c) Specific capacities of HG1300 and DG1300 in comparison to reported carbon anodes for sodium-ion batteries; d) Rate performance at different current densities including 0.1, 0.2, 0.5, 1.0, and 2.0 C, and e) Cycling performance at 0.5 C, of HG1300 and DG1300.

samples in each series from a performance perspective. Besides, the solid electrolyte interphase (SEI) formation mainly results in the irreversible capacity during the first cycle, thus leading to a decrease in the initial Coulombic efficiency (ICE).[34] The ICE of HG1300 and DG1300 both can reach as high as 85%. However, the ICE is much lower for HG1000 and DG1000 which were carbonized at the relatively low temperature of 1000 °C because of extensive SEI formation on the abundant open pores (Table S1, Supporting Information).[35] In a full cell, a higher ICE means less consumption of sodium ions from the cathode to form excessive SEI at the anode side, which can therefore reduce the mass of the cathode needed in the full-cell configuration.[36]

In Figure 2b, the sloping capacity of each sample is distinguished from its plateau capacity. When the carbonization temperature increases from 1000 to 1500 °C, the decrease in the contribution of sloping regions can be correlated to fewer defect sites in carbons for either HG or DG series, indicating that the sloping region may correspond to the adsorption of sodium ions at defect sites, in good agreement with our and others' previous observations.[9,13,23,28] Meanwhile, the samples of HG series carbonized at over 1300 °C have higher plateau capacities than the DG series, which is consistent with more closed nanovoids in HG1300 and HG1500 as described above.[23] A more detailed discussion on the sodium-ion storage sites in the different carbon materials will be presented in the following section using kinetic analysis, advanced characterization, and simulations. As the most promising hard

carbon material in this study, the capacity of HG1300 is also highly competitive to other reported carbonaceous materials for sodium-ion storage (Figure 2c), ranking within the top level of state-of-the-art carbon anodes.[9,37–41] For the rate performance (Figure 2d) ranging from 0.1 C to 2.0 C, the retention of the capacity of spherical HG1300 at 2.0 C is 31.1%, which is much higher than that of DG1300 (14.7%). Thus, the imbalance between the kinetics of anodes and cathodes will be exacerbated by the poor rate performance of DG1300. When the current density returns to 0.1 C, the capacity of HG1300 is able to recover to its original level, further proving the reversibility and stability of the HG material. For the cycling performance at 0.5 C (Figure 2e), HG1300 with an average decay rate below 0.09% each cycle has higher capacity retention after 300 cycles than DG1300 whose cell fails after around 250 cycles. The cycling performance of DG1300 and HG1300 was continuously tested after the rate performance testing. Hence, the obvious difference in the performance of DG1300 at 0.5 C between Figure 2d,e can further prove the instability of DG1300 for sodium-ion storage. Furthermore, the half-cell of HG1300 with an ultra-long lifetime can run for about 1000 cycles at 0.5 C (Figure S8, Supporting Information). Detailed electrochemical performance of all samples is presented in Figure S9, Supporting Information. In brief, the defects and closed nanovoids of HG1300 provide more sodium-ion storage sites, and the hierarchical pore structure of HG1300 and its compact packing density based on spherical particles enhances the mass and charge transfer. These beneficial properties are a direct result
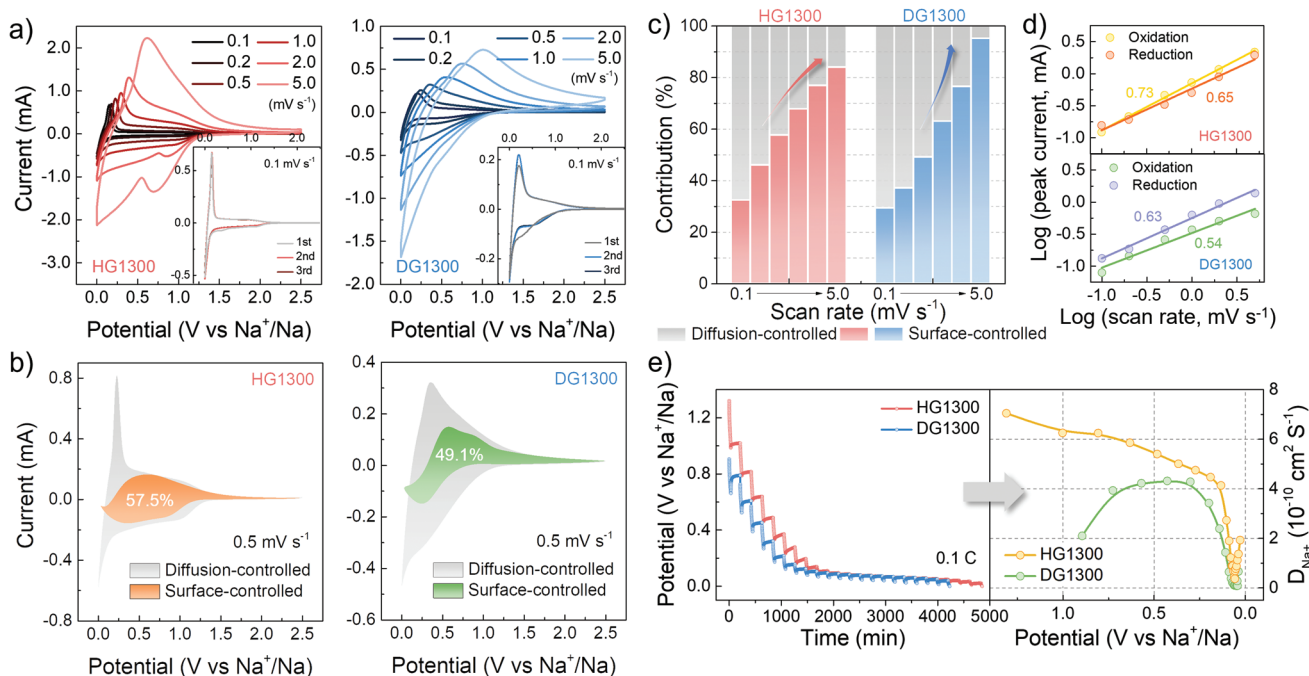
Figure 3. Kinetic analysis. a) CV curves of HG1300 and DG1300 at different scan rates of 0.1, 0.2, 0.5, 1.0, 2.0, and 5.0 mV s^{-1} (the second cycle at each scan rate), inserted with the very first three cycles of CV curves of HG1300 and DG1300 at 0.1 mV s^{-1}; b) The surface-controlled current separated from the diffusion-controlled one at each potential in CV curves of HG1300 and DG1300 at 0.5 mV s^{-1}; c) Calculated contributions of the surface- and diffusion-controlled proportions varying from 0.1 to 5.0 mV s^{-1} in HG1300 and DG1300; d) Linear relationship between log (peak current) and log (scan rate) of HG1300 and DG1300 for calculating the exponent (b values) in half cells based on Equation (S4); e,f) GITT profiles of HG1300 and DG1300 (left) by discharging the half cells with a pulse current at 0.1 C for 30 min followed by an interval for 3 h, and calculated D_{Na+} (right) at different potentials.

of the hydrothermal pre-treatment, enabling the excellent electrochemical performance of HG1300.

2.3. Electrochemical Kinetic Calculation and Analysis

Cyclic voltammetry (CV) measurements of hard carbons in the half-cell configuration from 0.1 to 5.0 mV s^{-1} can be employed to investigate the detailed electrochemical reactions and their corresponding kinetics. The formation of SEI introduces irreversibility in the CV profiles from the first cycle (insets in **Figure 3**a). In Figure 3a, HG1300 and DG1300 exhibit different CV curves at increased scan rates because the electrochemical kinetics of HG1300 differ from DG1300. With the increase in scan rates, DG1300 has more potential shift of redox peaks and polarization of CV profiles than HG1300. Under 5.0 mV s^{-1}, the CV curve of HG1300 still displays sharp redox peaks, while redox peaks of DG1300 become broad and tend to diminish. Furthermore, the redox peak in CV curves (Figure 3a) corresponds to the plateau region in GCD curves (Figure 2a). In comparison to DG1300, the sharper redox peaks in the CV curves of HG1300 (Figure 3a) represent the lower potential range of the plateau region in the GCD curves of HG1300 (e.g., below 0.1 V vs Na$^+$/Na at 0.1 C) (Figure 2a), which means a higher average working voltage in the full-cell configuration using HG1300.

To understand these differences in CV curves, the currents contributed by surface- or diffusion-controlled reactions are calculated based on Equations S4 and S5, Supporting Information. The response currents in the sloping region are

mainly composed of the surface-controlled currents, and the diffusion-controlled currents dominate in the plateau region (Figure 3b). From a kinetic point of view, the surface-controlled reaction in the sloping region with a faster kinetic is similar to the pseudocapacitive process due to the adsorption of sodium ions on the surface or near-surface active sites in the form of defects.[26] In contrast, the diffusion-controlled reaction in the plateau region is attributed to the diffusion and storage of cations in the carbon bulk phase with slower kinetics.[26] According to Figure 3c, most of the capacity (around 70%) at a low scan rate (0.1 mV s^{-1}) is provided by the diffusion-controlled reactions in the plateau region, which is a typical feature of high-energy battery-type hard carbon anodes. During a faster charge-discharge process, the loss of capacity is manifested by the decrease in diffusion-controlled reactions in the plateau region, which simply do not have time to occur. As the scan rate increases from 0.1 to 5.0 mV s^{-1}, the contribution of surface-controlled reactions in HG1300 slowly rises from 32.4 to 84.0%, but that in DG1300 rapidly grows from 29.4 to 95.2% (Figure 3c). Together with the more obvious disappearances of DG1300 redox peaks at an increased scan rate, this tendency can also be related to the poorer rate performance of DG1300 described before. Furthermore, based on Equation S4, Supporting Information, the b-values of the reduction and oxidation peaks of HG1300 are 0.65 and 0.73, respectively, both higher than those of DG1300 (0.63 and 0.54) (Figure 3d); hence, the kinetics of diffusion-controlled reactions in HG1300 are faster than those in DG1300, which explains the better rate performance of HG1300. Overall, the hydrothermal pre-treatment not only produces more active sites to enhance the

surface- and diffusion-controlled capacities but also creates interconnected spherical morphologies and hierarchical pore structures in HG1300 to facilitate the ion and electron diffusion, thus enabling excellent electrochemical kinetics.

To further understand the electrochemical kinetics of hard carbons, the galvanostatic intermittent titration technique (GITT) can be utilized to evaluate the diffusion coefficient of sodium ions (D_{Na+}) in the electrode during the second discharge process (Equation S6, Supporting Information). In Figure 3e, the calculated D_{Na+} of HG1300 slightly decreases in the sloping region of the sodiation process, followed by a rapid decrease in the plateau region. This situation also validates that when the potential decreases from the sloping region to the plateau region, the electrochemical reactions switch from surface-controlled to diffusion-controlled. Compared with HG1300, the average D_{Na+} of DG1300 in the sloping region is not notably higher than that in the plateau region, although differences in the two regions still exist. Similar trends can also be observed in the GITT profiles of other samples at different carbonization temperatures (Figure S11, Supporting Information). The kinetics of their electrochemical reactions in sloping and plateau regions elucidated here can, therefore, attest that the sloping region is based on the faster adsorption of sodium ions on the superficial active sites like defects.[42] In contrast, the plateau region refers to the slower diffusion and storage of sodium ions at active sites like closed nanopores within the bulk phase of carbons.[9]

2.4. Fundamental Mechanistic Insights Into Sodium-Ion Insertion Behaviors and Interfacial Phenomena

To further evaluate the relationship between active sites in hard carbons and electrochemical behaviors, high-resolution operando Raman spectroscopy including characteristic peaks and the low-frequency Raman shift region was conducted to understand the detailed sodium-ion storage mechanisms in HG1300 (**Figure 4**a and Figure S12a, Supporting Information). The operando Raman spectroscopy setup is presented in Figure 4a and Figure S12, Supporting Information, where the Raman beam (532 nm) was continuously focused on a fixed particle of HG1300 during the discharge-charge process. The first Raman spectrum of HG1300 has typical broad D- and G-peaks (Figure 4a), which is the same as Figure 1g. Likewise, the low-frequency Raman signal cannot be observed at the very beginning of the electrochemical sodium-ion storage process, and the basic intensity here is the background signal caused by the Rayleigh scattering. In detail, the first-order Raman scattering from a phonon in the plane of crystalline graphene layers leads to the G-peak at ≈1580 cm^{-1}, which is also called the E_{2g} in-plane bond-stretching motion of pairs of sp^2 carbon atoms (Figure S12b, Supporting Information).[43] The D-peak at ≈1350 cm^{-1} refers to the A_{1g} breathing mode of sp^2 carbon atoms (Figure S12c, Supporting Information).[32] The relative motion of graphene planes (i.e., the distortion and dislocation of graphene planes) from the shear mode will lead to changes in low-frequency Raman signal below 200 cm^{-1}.[20]

In the sloping region (>0.1 V vs Na$^+$/Na), the D-peak becomes broader and slightly shifts to a lower wavenumber, which indicates sodium ions are interacting with defect sites (e.g., carbon vacancies, substitutional and interstitial impurities, etc.), thus restricting A_{1g} breathing mode of D-band (Figure S12c, Supporting Information).[44] The position of the G-band peak remains almost unchanged in this region, suggesting no sodium ion significantly reacts with sp^2 carbon atoms because the E_{2g} stretching mode of G-band is highly sensitive to ion doping.[45] Meanwhile, the low-frequency Raman signal responsive to the plane de-coupling is still not observed, further implying that sodium ions' interaction with defect sites belongs to the adsorption mode without any evident inner shearing (Figure 4b).[20] Consequently, the adsorption mode of sodium ions at defect sites as the surface-controlled reaction dominates in the sloping region, and the fast electrochemical kinetics in this region can also be explained by this phenomenon.

During the plateau region (<0.1 V vs Na$^+$/Na), the D-peak becomes broader and shifts to a lower wavenumber. This implies that the interaction between sodium ions and defect sites still exists.[44] As observed above, the surface-controlled currents in this region can also be correlated to the existence of adsorbing sodium ions at defect sites. Nevertheless, the decrease in the G-band peak position can be observed along with an increase in its width in the plateau region, which means the length of the C−C bonds is changed by the charge transfer from sodium atoms to π^* antibonding orbitals of carbon atoms.[45] Namely, sodium ions diffuse to suitable inner voids enclosed by curved graphene layers and interact with sp^2 carbon atoms, thus affecting the E_{2g} stretching mode of the G-band (Figure S12b, Supporting Information).[43] Notably, the sharp low-frequency Raman feature is now observed. During the plateau region, the intensity of the low-frequency Raman signal becomes stronger, and its position also increases by 15 cm^{-1}. This trend provides further evidence that the reaction of sodium ions within closed nanovoids via a kind of filling and expansion mode by interacting with more accessible sp^2 carbon atoms; this reaction increases the inner shearing stress and disordered degree of the carbon bulk phase via the dislocations of graphene planes (insets in Figure 4b).[20] As this reaction continues in the filling mode, the E_{2g} stretching mode of G-band is eventually significantly suppressed (Figure S12b, Supporting Information). By linking the structural changes observed in this section with the previous kinetic analysis, we can conclude that this filling mode of sodium ions into closed nanovoids needs to overcome large energy barriers, and proceeds with slow kinetics as the diffusion-controlled reaction.

For the duration of the de-sodiation process, D- and G-band peaks both gradually shift back towards their original position, and the low-frequency Raman signal decreases, combined with the steady recovery of their widths, which suggests the reversibility of the sodium-ion storage behaviors as well as the structural stability of HG1300. In Figure 4b, compared with HG1300, DG1300 which is less defective with narrower nanovoids, hence, can accommodate fewer sodium ions.

In addition to operando Raman spectra, electrochemical impedance spectroscopy (EIS) (Figure 4c) and ex situ XPS (Figure 4d,e) of cycled HG1300 and DG1300 at the same de-sodiated state are used to analyze the interface conditions. According to the slope differences in the low-frequency regions of HG1300 and DG1300 (Figure 4c), the ion diffusion in
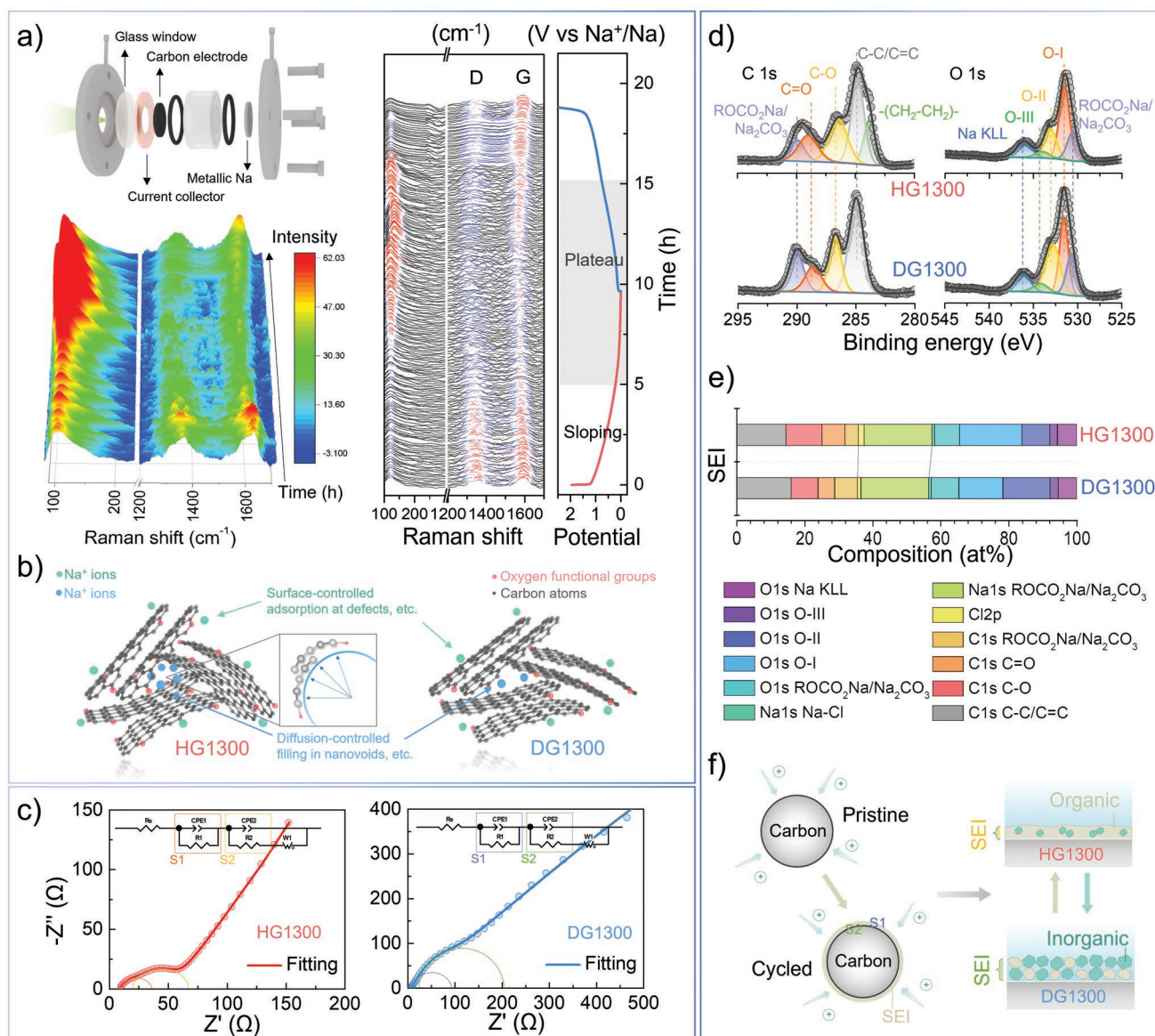
Figure 4. Operando and ex situ characterizations. a) Operando Raman spectra of HG1300 and the corresponding 3D mapping image during the second discharge-charge process using the illustrated operando Raman cell; b) Schematic illustrations of the sodium-ion storage behaviors in HG1300 and DG1300 with different structural features; c) Fitted EIS of cycled HG1300 and DG1300 at the same de-sodiated state based on the modified equivalent circuits with two charge-transfer resistances in two phases (S1 and S2); d) Fitted C 1s (left) and O 1s (right) core level XPS spectra of HG1300 and DG1300 after the first discharge-charge process; e) Corresponding composition contributions of the interphase upon de-sodiated HG1300 and DG1300; f) Schematic diagrams of the interface conditions of cycled carbons (left) with detailed illustrations of possible SEI compositions upon cycled HG1300 and DG1300 (right).

liquid and capacitive accumulation on HG1300 are faster.[46] At the de-sodiated state, as SEI fully covers the carbon surface, the charge must transfer through two interphases before reaching the current collector. One is the transfer within SEI (S1), and the other is the transfer within carbons (S2) (Figure 4f). Therefore, the small curved feature is composed of two separate semicircles in the high-frequency region.[47] By fitting the Nyquist plot based on Equation S7, Supporting Information, two different charge-transfer resistance (R_{ct}) parts of HG1300 can be individually achieved (Table S2, Supporting Information), whose values are both smaller than those of DG1300. In addition, the HG series all have smaller equivalent series resistance (ESR) than the DG series (Figure S13, Supporting Information). The smaller R_{ct} of S2 of HG1300 results from its spherical morphology and hierarchical pore structures resulting from the hydrothermal pre-treatment. Especially, the smaller R_{ct} of S1 of HG1300 suggests the thinner SEI layer upon HG 1300 with the better ionic conductivity, compared with DG1300.

Furthermore, the ionic conductivity of SEI is related to its composition, which is evaluated by ex situ XPS here. The ex situ XPS study was performed after the first discharge-charge process. A vacuum transfer capsule was used to load the

samples from the glovebox to the XPS facility to protect the samples from surface contamination. After fitting C 1s, O 1s, Na 1s, and Cl 2p core-level XPS spectra of the cycled samples (Figure 4d and Figure S14, Supporting Information), the atomic composition of the SEI layer is unveiled (Figure 4e). The peaks of C−C/C=C ($\approx$284.8 eV), C−O ($\approx$287.0 eV), C=O ($\approx$288.6 eV), and Na$_2$CO$_3$/ROCO$_2$Na ($\approx$290.0 eV) can be observed in both HG1300 and DG1300. Second, the peaks of O-I ($\approx$531.5 eV), O-II ($\approx$532.5 eV), O-III ($\approx$534.5 eV), and Na$_2$CO$_3$/ROCO$_2$Na ($\approx$530.5 eV) can be identified in O 1s core-level XPS spectra. For the SEI layers on the surface of HG1300 and DG1300 (Figure 4e), both are a mixture of organics and inorganics. However, the calculated proportions of organics ($\approx$ 66.3 at%), are dominant in the SEI layer of HG1300 according to fitted XPS spectra, which is higher than that of DG1300 ($\approx$ 58.1 at%). As a result, the formed SEI on HG1300 may be expected to exhibit better flexibility. Such a kind of SEI layer model supported by the organic phase (Figure 4f) can enhance the interface stability and, reasonably, the ionic conductivity upon cycling,[48,49] which can be correlated with the better cycling performance of HG1300 described before. In contrast, composed of more inorganic components, a kind of mosaic model can be established for the SEI of DG1300 whose extra inorganic compositions with more ceramic features are fragile and brittle during cycling (Figure 4f).[49,50]

In the same electrolyte, the discrepancies in the SEI components can be attributed to the differences in the electrostatic interactions of carbon surfaces with the solvent molecules, which can be estimated using molecular modeling. The obtained electrostatic potential maps of electrolyte molecules (**Figure 5**a) show that the negative charge region (red) is mainly concentrated on the oxygen atoms of C=O groups of EC, followed by the polarization of EC into a local dipole.[51] At the same time, oxygen atoms in the functional groups can delocalize the charges on carbon atoms to form a positive charge region, namely another local dipole. Based on the previous XPS characterization, HG1300 has more enriched oxygen functional groups than DG1300. Therefore, HG1300 has more possibility to form the local dipoles. These local dipoles between carbons and organic solvent molecules can strongly interact with each other (Figure 5a) to induce a more homogenous decomposition of organic solvent molecules on the surface of HG1300.[51]

In addition, the finite element simulation taking material morphologies into account was also performed to assess the uniformity of the ion flux, which can affect the electrolyte decomposition and sodium ion diffusion (Figure 5b). The 2D electric field distributions around HG1300 and DG1300 are first presented in Figure 5c. The blue substrates represent carbons with two different surface scenarios, and the colorful areas surrounding the substrate are defined as the changes of the electric field distributions. Hence, the electric field distribution can represent the voltage change rate with various ion flux densities. In Figure 5c, the spherical morphology of HG1300 can homogenize the ion flux to stabilize the interface condition. At the same time, the sharp tips on the irregular morphology of DG1300 can lead to uneven electric field distributions,[52] which will be very dangerous during the fast charge-discharge process. The concentrated ion flux around DG1300 can result in the precipitation and random nucleation of metallic sodium during

the fast charge-discharge process, thus forming uncontrollable sodium dendrites in the end.[44] Moreover, the 3D electric field distributions and voltage changes around HG1300 are further simulated to comprehensively predict the ion flux of HG1300 (Figure 5d). The grey substrate represents HG1300 in the 3D simulation. Differing from the ideal 2D model, the ion flux will concentrate on the top of HG1300 spheres to some extent in the 3D model under a vertically applied voltage. In short, the homogenous ion flux and uniform voltage change can be still observed in Figure 5d, which benefits from the spherical morphology of HG1300. A more ordered morphology leads to a more predictable ion flux. The 3D model further proves the advantages of structural pre-stabilization using hydrothermal pre-treatment.

2.5. Life Cycle Assessment of Hard Carbon Anodes for Sodium-Ion Storage

We have shown that the hydrothermal pre-treatment can improve the performance and stability of hard carbons for sodium-ion batteries. In addition to the electrochemical performance, it is equally of great significance to evaluate the sustainability of hard carbons from the hydrothermal process for sodium-ion batteries. LCA studies have been widely used to study the hydrothermal process of different feedstocks for applications like bioenergy production, heat, and electricity production.[53,54] However, the LCA study on hydrothermal carbons for energy storage is non-existent and urgently needed, in particular for sodium-ion batteries. Hence, based on the standard of ISO 14040:2006 and the databases of Product Environmental Footprints (PEF) and Ecoinvent,[55] an innovative LCA study can be conducted using openLCA software to demonstrate the sustainability of the hydrothermal process of biomass for the battery technology beyond lithium. The detailed inventory data used for LCA are listed in Table S3, Supporting Information.

As shown in Figure 5e, the hydrothermal process, the subsequent carbonization and the wastewater treatment are individually defined in the route for HG1300. Meanwhile, the direct carbonization is also defined in the route for DG1300. According to Figure 2a and Figure 5f, the additional hydrothermal process not only enhances the specific capacity from 261.3 to 347.4 mAh g^{-1} but also increases the carbon yield from 18.9 to 26.0%, which makes a significant impact at larger scales. Here, the life cycle impact (LCI) assessment is calculated to show the five main environmental impact factors of the two different scenarios at the kilogram (kg) level, including global warming potential (GWP), acidification potential (AP), eutrophication potential (EP), human toxicity potential (HTP), and photochemical oxidants creation potential (POCP), using the CML 2001 method.[56] First of all, the theoretical specific capacity of graphite anodes in lithium-ion batteries is 372 mAh g^{-1}. Hence, the capacity of 1 kg of graphite anodes for lithium (372 Ah) is equal to the capacity of 1.07 kg of HG1300 or 1.42 kg of DG1300 for sodium according to their measured specific capacities, which enables us to normalize and standardize the comparison between our samples and commercial graphite. Furthermore, based on their carbon yields, the glucose resource required by HG1300 and DG1300 are 4.12 and 7.51 kg, respectively, for
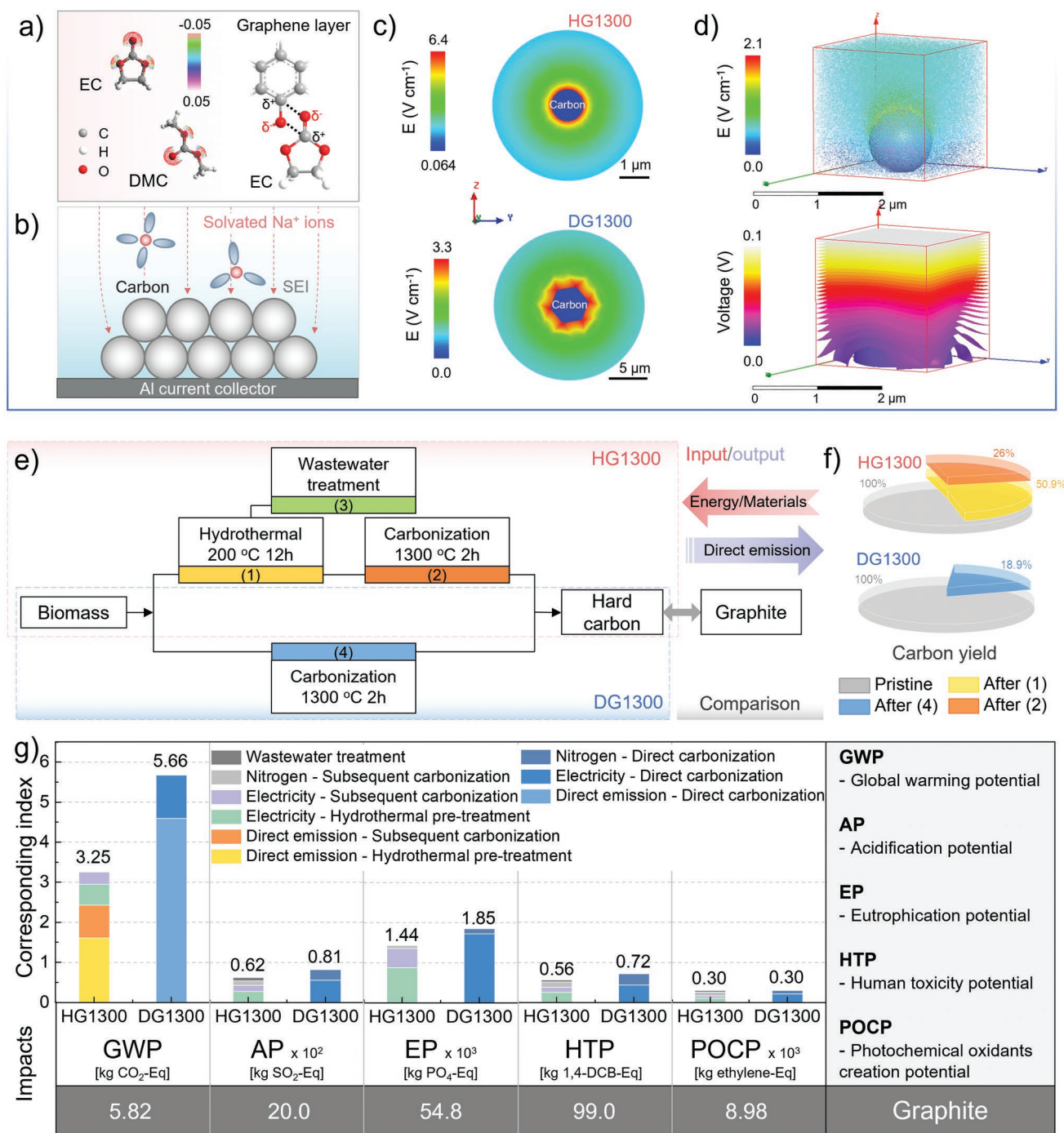
Figure 5. Modeling and assessment. a) Electrostatic potential mapping of EC and DMC with the dipole-dipole interaction between EC and oxygen functional groups of carbons; b) The schematic illustration of the uniform sodium-ion flux from the electrolyte to carbon spheres; c) 2D electric field distribution vector profiles of the sodium-ion flux from the electrolyte to spherical HG1300 and lumpy DG1300 under a constant electric field of 0.1 V; d) The 3D electric field distribution vector profile and voltage change profile of the sodium-ion flux from the electrolyte to spherical HG1300 under a constant electric field of 0.1 V. e) The life cycle diagram of the preparation of hard carbons from the same precursor via two different routes for sodium-ion batteries, compared with graphite for lithium-ion batteries; f) The measured carbon yields at different stages of routes for HG1300 and DG1300; g) The calculated environmental impacts of hard carbons including HG1300 and DG1300 from two different routes for sodium-ion batteries, compared with those of graphite for lithium-ion batteries.

the production of hard carbons with the standard capacity of 372 Ah.

Figure 5g and Table S4, Supporting Information, show the calculated environmental impact factors of HG1300 and DG1300 for sodium-ion batteries. The GWPs of HG1300 and DG1300 are 3.25 and 5.66 kg CO_2 eq kg^{-1}, respectively. Among them, the direction carbon emissions per kg of HG1300 (2.43 kg CO_2 eq kg^{-1}) are much lower than those of DG1300

2200208 (10 of 13)

(4.59 kg CO_2 eq kg^{-1}). Moreover, the GWPs generated by the electricity of the hydrothermal process (0.52 kg CO_2 eq kg^{-1}) and subsequent carbonization (0.30 kg CO_2 eq kg^{-1}) for HG1300 is also lower than that for DG1300 (1.08 kg CO_2 eq kg^{-1}). Hence, even though the hydrothermal pre-treatment represents an extra step in the preparation of HG1300, its energy consumption and resulting carbon emissions are lower than those of the one-step carbonization for DG1300. These trends all result from the increased carbon yield and enhanced specific capacity of HG1300 contributed by the hydrothermal pre-treatment. In addition, compared with the GWP of graphite (5.82 kg CO_2 eq kg^{-1}),[55] HG1300 can also deliver the same capacity with lower GWP (3.25 kg CO_2 eq kg^{-1}). Therefore, introducing the hydrothermal pre-treatment into the synthesis route makes the preparation of HG1300 more sustainable when it comes to the GWP factor. In terms of other impact factors such as AP, EP, HTP, and POCP, these impact factors can be mainly ascribed to the input of electricity, implying that a higher energy input usually leads to a higher calculated environmental impact factor. Still, compared to graphite, the impact factors of the two scenarios are all reduced by over 95%, which further proves the importance of using renewable precursors and waste recycling towards carbon neutrality in the future. Combined with our reported LCA studies of the hydrothermal process of other feedstocks (e.g., cellulose, etc.) for sodium-ion batteries,[55] we

can conclude that the hydrothermal process is a necessary step to pre-treat biomass for sodium-ion batteries, which will result in better environmental impacts than the direct carbonization of biomass or the production of commercial graphite at scale.

2.6. Practical Applications of Sodium-Ion Full Cells

To fully evaluate the potential of our hard carbon anodes in practical applications, sodium-ion full cells were also assembled by coupling the hard carbon anode with a $Na_3V_2(PO_4)_3$ (NVP) cathode (**Figure 6**a). From Figure 6b in the half-cell configurations, the specific discharge capacity of HG1300 is 420 mAh g^{-1}, while the specific charge capacity of NVP is 120 mAh g^{-1}. Therefore, the active mass of electrodes is adjusted to make the capacity ratio of the negative to positive electrodes (N/P ratio) around 1.1, which can maximize the energy and power of full-cells and the stability,[57] When a good balance between HG1300 anode and NVP cathode is achieved, a full cell made of HG1300//NVP with the highest capacity can be fabricated, where the reversible capacity of the full cell is 318.2 mAh g^{-1} at the current density of 30 mA g^{-1} normalized by the active mass of the anode (Figure 6c). The average working voltage is 3.5 V. The shape of the GCD curves of HG1300//NVP (Figure 6c) reflects the combination of
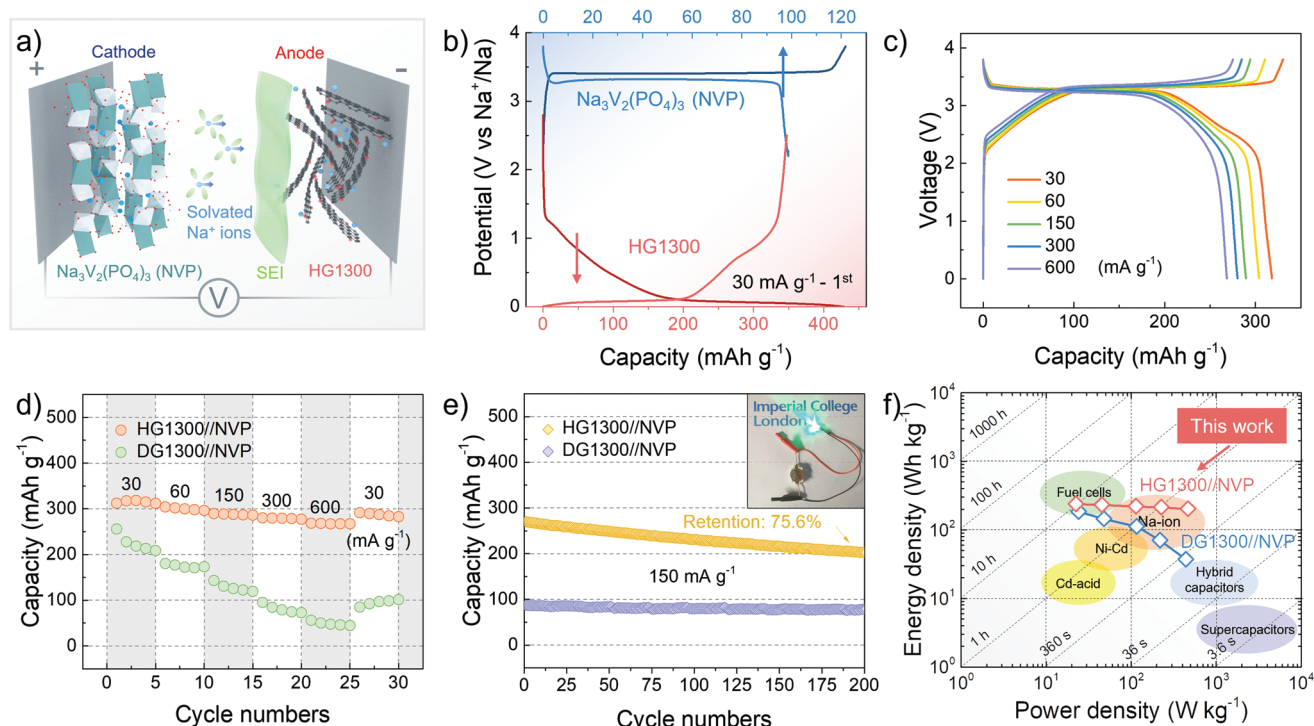
Figure 6. Full cells. a) The schematic illustration of the full configuration, where the hard carbon anode is coupled with the $Na_3V_2(PO_4)_3$ cathode during the charge process; b) The first charge-discharge cycles of the hard carbon anode and the $Na_3V_2(PO_4)_3$ cathode in their half-cell configurations at the same current density; c) GCD curves of the full-cell using the HG1300 anode and the $Na_3V_2(PO_4)_3$ cathode (HG1300//NVP) at the current densities of 30, 60, 150, 300, and 600 mA g^{-1}, whose capacities are normalized by the active mass of the anode; Comparison of d) the rate performance at the current densities of 30, 60, 150, 300, and 600 mA g^{-1}, and e) the cycling performance at 150 mA g^{-1}, between HG1300//NVP and DG1300//NVP whose capacities are normalized by the active mass of the anode, with an inserted image of a LED light powered by the full cell of HG1300//NVP; f) The Ragone plot to compare the energy and power densities of our full cells with other types of energy storage devices, where the energy and power densities are normalized by the overall active mass of both the anode and cathode.

synergetic electrochemical reactions between HG1300 and NVP, where the plateau and sloping regions of the full cell correspond to the plateau and sloping regions of HG1300. Along with increased current densities of 60, 150, 300, and 600 mA g^{-1}, the capacity of the full-cell becomes 304.1, 289.5, 280.2, and 268.5 mAh g^{-1}, respectively (Figure 6d), suggesting an excellent rate performance and ability to fast-charge. When the current density is reversed back to 30 mA g^{-1}, the capacity shows excellent reversibility and reaches the original value. In comparison, the full cell of DG1300//NVP exhibits a lower initial capacity of 255.7 mAh. g^{-1} and an inferior rate performance with a capacity retention of only 17.4% (Figure 6d and Figure S15, Supporting Information) as a result of the poor electrochemical performance of DG1300. Additionally, when the current density returns to 30 mA g^{-1}, the capacity cannot recover to the initial capacity. After 200 cycles at 150 mA g^{-1}, the capacity retention of the HG1300//NVP full cell is 75.6% (Figure 6e). From the inset in Figure 6e, the green LED light can be successfully powered by an HG1300//NVP full cell even after 200 cycles, which further demonstrates the full cell's excellent stability. Finally, the calculated energy and power densities of HG1300//NVP and DG1300//NVP are presented in Figure 6f. For HG1300//NVP, the energy densities can reach 237.8, 230.2, 219.4, 211.9, and 201.5 Wh kg^{-1} when the power densities are 22.6, 45.6, 114.5, 227.8, and 468.6 W kg^{-1}, respectively, which are much higher than those of DG1300//NVP. The full-cell configuration therefore further confirms the importance of the hydrothermal pre-treatment for bio-derived carbon anodes. In addition, the energy and power densities of HG1300//NVP are superior to other energy devices, while also being very competitive with those state-of-the-art sodium-ion batteries (Table S5, Supporting Information). Generally, this work successfully paves the way for the next-generation sodium-ion batteries using the hydrothermal bio-derived carbons. By coupling our anode with a sodium layered metal oxide cathode, the energy and power of the full cell can be further enhanced close to the commercial lithium-ion batteries.

3. Conclusions

In this work, for the first time, we provide a comprehensive understanding of the critical role played by the hydrothermal carbonization process in designing sustainable sodium-ion battery anodes by comparing two different scenarios with and without a hydrothermal pre-treatment. By correlating the structural differences in hard carbons with their electrochemical sodium-ion storage behaviors, the extra active sites including defects and nanovoids introduced by the hydrothermal pretreatment are responsible for the enhanced electrochemical performance in sodium-ion batteries. Based on the electrochemical kinetic analysis and operando measurements, a modified sodium-ion storage mechanism in hard carbons is unveiled in detail. Precisely, the adsorption mode of sodium ions at defect sites in the whole region, especially in the sloping region, can be confirmed. In contrast, the filling mode of sodium ions at nanovoids in the plateau region can be demonstrated through operando Raman spectroscopy of hard carbons. Using a combination of ex situ characterization and multi-scale

modeling, we also obtain fundamental insights into sodium-ion diffusion behaviors and interfacial phenomena including the SEI compositions, which confirm the benefits of the spherical morphology and hierarchical pore structures to the uniform ion flux as well as the functions of surface oxygen groups for the homogenous interface characteristics. Along with the exceptional performance metrics, the sustainability of material synthesis and battery application is also considered from a life cycle perspective. The LCA is innovatively used to quantify the superior sustainability of bio-derived hard carbons for sodium-ion batteries. The hydrothermal carbonization process is shown to pre-stabilize the carbon morphologies and structures, increasing the overall carbon yield and decreasing the carbon emission simultaneously. In conclusion, the hydrothermal carbonization process is a useful step to pre-treat biomass and produce advanced hard carbons with real sustainability and enhanced performance for sodium-ion batteries, thereby providing a promising opportunity for the development of next-generation sustainable batteries beyond lithium.

Supporting Information

Supporting Information is available from the Wiley Online Library or from the author.

Conflict of Interest

The authors declare no conflict of interest.

Data Availability Statement

The data that support the findings of this study are available from the corresponding author upon reasonable request.

[1] R. Usiskin, Y. Lu, J. Popovic, M. Law, P. Balaya, Y.-S. Hu, J. Maier, *Nat. Rev. Mater.* **2021**, *6*, 1020.

[2] C. Vaalma, D. Buchholz, M. Weil, S. Passerini, *Nat. Rev. Mater.* **2018**, *3*, 18013.

[3] W. Luo, F. Shen, C. Bommier, H. Zhu, X. Ji, L. Hu, *Acc. Chem. Res.* **2016**, *49*, 231.

[4] H. S. Hou, X. Q. Qiu, W. F. Wei, Y. Zhang, X. B. Ji, *Adv. Energy Mater.* **2017**, *7*, 1602898.

[5] F. Xie, Z. Xu, Z. Guo, Y. Lu, L. Chen, M.-M. Titirici, Y.-S. Hu, *Sci. China: Chem.* **2021**, *64*, 1679.

[6] X. Dou, I. Hasa, D. Saurel, C. Vaalma, L. Wu, D. Buchholz, D. Bresser, S. Komaba, S. Passerini, *Mater. Today* **2019**, *23*, 87.

[7] D. A. Stevens, J. R. Dahn, *J. Electrochem. Soc.* **2000**, *147*, 4428.

[8] M. M. Titirici, R. J. White, N. Brun, V. L. Budarin, D. S. Su, F. del Monte, J. H. Clark, M. J. MacLachlan, *Chem. Soc. Rev.* **2015**, *44*, 250.

[9] Y. M. Li, Y. S. Hu, M. M. Titirici, L. Q. Chen, X. J. Huang, *Adv. Energy Mater.* **2016**, *6*, 1600659.

[10] E. Goikolea, V. Palomares, S. Wang, I. R. Larramendi, X. Guo, G. Wang, T. Rojo, *Adv. Energy Mater.* **2020**, *10*, 2002055.

[11] M.-M. Titirici, *Adv. Energy Mater.* **2021**, *11*, 2003700.

[12] J. Y. Hwang, S. T. Myung, Y. K. Sun, *Chem. Soc. Rev.* **2017**, *46*, 3529.

[13] Y. Y. Huang, Y. H. Zheng, X. Li, F. Adams, W. Luo, Y. H. Huang, L. B. Hu, *ACS Energy Lett.* **2018**, *3*, 1604.

[14] B. Hu, K. Wang, L. Wu, S. H. Yu, M. Antonietti, M. M. Titirici, *Adv. Mater.* **2010**, *22*, 813.

[15] M.-M. Titirici, R. J. White, C. Falco, M. Sevilla, *Energy Environ. Sci.* **2012**, *5*, 6796.

[16] F. Xie, Z. Xu, Z. Guo, M.-M. Titirici, *Prog. Energy* **2020**, *2*, 042002.

[17] Z. Zhu, Z. Xu, *Renewable Sustainable Energy Rev.* **2020**, *134*, 110308.

[18] A. B. Jorge, R. Jervis, A. P. Periasamy, M. Qiao, J. Feng, L. N. Tran, M. M. Titirici, *Adv. Energy Mater.* **2019**, *10*, 1902494.

[19] C. Hu, Y. Lin, J. W. Connell, H. M. Cheng, Y. Gogotsi, M. M. Titirici, L. Dai, *Adv. Mater.* **2019**, *31*, 1806128.

[20] H. Yadegari, M. A. Koronfel, K. Wang, D. B. Thornton, I. E. L. Stephens, C. Molteni, P. D. Haynes, M. P. Ryan, *ACS Energy Lett.* **2021**, *6*, 1633.

[21] J. Peters, D. Buchholz, S. Passerini, M. Weil, *Energy Environ. Sci.* **2016**, *9*, 1744.

[22] S. A. Nicolae, H. Au, P. Modugno, H. Luo, A. E. Szego, M. Qiao, L. Li, W. Yin, H. J. Heeres, N. Berge, M.-M. Titirici, *Green Chem.* **2020**, *22*, 4747.

[23] H. Au, H. Alptekin, A. C. S. Jensen, E. Olsson, C. A. O'Keefe, T. Smith, M. Crespo-Ribadeneyra, T. F. Headen, C. P. Grey, Q. Cai, A. J. Drew, M.-M. Titirici, *Energy Environ. Sci.* **2020**, *13*, 3469.

[24] P. Modugno, M. M. Titirici, *ChemSusChem* **2021**, *14*, 5271.

[25] K. Tang, L. J. Fu, R. J. White, L. H. Yu, M. M. Titirici, M. Antonietti, J. Maier, *Adv. Energy Mater.* **2012**, *2*, 873.

[26] Z. Xu, F. Xie, J. Wang, H. Au, M. Tebyetekerwa, Z. Guo, S. Yang, Y. S. Hu, M. M. Titirici, *Adv. Funct. Mater.* **2019**, *29*, 1903895.

[27] S. A. Nicolae, J. Louis-Therese, S. Gaspard, P. Á. Szilágyi, M. M. Titirici, *Nano Select* **2021**, *3*, 165.

[28] F. Xie, Z. Xu, A. C. S. Jensen, H. Au, Y. Lu, V. Araullo-Peters, A. J. Drew, Y. S. Hu, M. M. Titirici, *Adv. Funct. Mater.* **2019**, *29*, 1901072.

[29] C. Casiraghi, A. C. Ferrari, J. Robertson, *Phys. Rev. B* **2005**, *72*, 085401.

[30] A. C. Ferrari, J. Robertson, *Phys. Rev. B* **2000**, *61*, 14095.

[31] A. C. Ferrari, J. C. Meyer, V. Scardaci, C. Casiraghi, M. Lazzeri, F. Mauri, S. Piscanec, D. Jiang, K. S. Novoselov, S. Roth, A. K. Geim, *Phys. Rev. Lett.* **2006**, *97*, 187401.

[32] A. C. Ferrari, D. M. Basko, *Nat. Nanotechnol.* **2013**, *8*, 235.

[33] E. Olsson, J. Cottom, Q. Cai, *Small* **2021**, *17*, 2007652.

[34] J. B. Goodenough, Y. Kim, *Chem. Mater.* **2010**, *22*, 587.

[35] F. Xie, Z. Xu, A. C. S. Jensen, F. Ding, H. Au, J. Feng, H. Luo, M. Qiao, Z. Guo, Y. Lu, A. J. Drew, Y.-S. Hu, M.-M. Titirici, *J. Mater. Chem. A* **2019**, *7*, 27567.

[36] H. He, D. Sun, Y. Tang, H. Wang, M. Shao, *Energy Storage Mater.* **2019**, *23*, 233.

[37] D. S. Bin, Y. M. Li, Y. G. Sun, S. Y. Duan, Y. X. Lu, J. M. Ma, A. M. Cao, Y. S. Hu, L. J. Wan, *Adv. Energy Mater.* **2018**, *8*, 1800855.

[38] D. F. Xu, C. J. Chen, J. Xie, B. Zhang, L. Miao, J. Cai, Y. H. Huang, L. N. Zhang, *Adv. Energy Mater.* **2016**, *6*, 1501929.

[39] H. Zhang, H. Ming, W. Zhang, G. Cao, Y. Yang, *ACS Appl. Mater. Interfaces* **2017**, *9*, 23766.

[40] Y. Zheng, Y. Wang, Y. Lu, Y.-S. Hu, J. Li, *Nano Energy* **2017**, *39*, 489.

[41] Y. Wen, K. He, Y. Zhu, F. Han, Y. Xu, I. Matsuda, Y. Ishii, J. Cumings, C. Wang, *Nat. Commun.* **2014**, *5*, 4033.

[42] C. Bommier, T. W. Surta, M. Dolgos, X. Ji, *Nano Lett.* **2015**, *15*, 5888.

[43] X. Li, J. Sun, J. Zhao, Y. Lai, X. Yu, Y. Liu, *Adv. Funct. Mater.* **2021**, *32*, 2106980.

[44] Z. Xu, Z. Guo, R. Madhu, F. Xie, R. Chen, J. Wang, M. Tebyetekerwa, Y.-S. Hu, M.-M. Titirici, *Energy Environ. Sci.* **2021**, *14*, 6381.

[45] J. S. Weaving, A. Lim, J. Millichamp, T. P. Neville, D. Ledwoch, E. Kendrick, P. F. McMillan, P. R. Shearing, C. A. Howard, D. J. L. Brett, *ACS Appl. Energy Mater.* **2020**, *3*, 7474.

[46] U. Krewer, F. Röder, E. Harinath, R. D. Braatz, B. Bedürftig, R. Findeisen, *J. Electrochem. Soc.* **2018**, *165*, A3656.

[47] P. Ge, S. Li, L. Xu, K. Zou, X. Gao, X. Cao, G. Zou, H. Hou, X. Ji, *Adv. Energy Mater.* **2019**, *9*, 1803035.

[48] Z. W. Seh, J. Sun, Y. Sun, Y. Cui, *ACS Cent. Sci.* **2015**, *1*, 449.

[49] J. Wang, Z. Xu, J. C. Eloi, M. M. Titirici, S. J. Eichhorn, *Adv. Funct. Mater.* **2022**, 2110862, https://doi.org/10.1002/adfm.202110862.

[50] X. Zheng, H. Fu, C. Hu, H. Xu, Y. Huang, J. Wen, H. Sun, W. Luo, Y. Huang, *J. Phys. Chem. Lett.* **2019**, *10*, 707.

[51] J. Bae, Y. Qian, Y. Li, X. Zhou, J. B. Goodenough, G. Yu, *Energy Environ. Sci.* **2019**, *12*, 3319.

[52] L. Ye, M. Liao, H. Sun, Y. Yang, C. Tang, Y. Zhao, L. Wang, Y. Xu, L. Zhang, B. Wang, F. Xu, X. Sun, Y. Zhang, H. Dai, P. G. Bruce, H. Peng, *Angew. Chem., Int. Ed.* **2019**, *58*, 2437.

[53] D. Iribarren, J. F. Peters, J. Dufour, *Fuel* **2012**, *97*, 812.

[54] A. Mohammadi, G. Venkatesh, M. Sandberg, S. Eskandari, S. Joseph, K. Granström, *Sustainability* **2020**, *12*, 9026.

[55] H. Liu, Z. Xu, Z. Guo, J. Feng, H. Li, T. Qiu, M. Titirici, *Philos. Trans. R. Soc., A* **2021**, *379*, 20200340.

[56] L. C. Dreyer, A. L. Niemann, M. Z. Hauschild, *Int. J. Life Cycle Assess.* **2003**, *8*, 191.

[57] J. Xiang, L. Yang, L. Yuan, K. Yuan, Y. Zhang, Y. Huang, J. Lin, F. Pan, Y. Huang, *Joule* **2019**, *3*, 2334.